

DAA, AMES

98944

R-FILE IN-05 - CR

**JOINT INSTITUTE FOR AERONAUTICS AND ACOUSTICS**

P. 40

National Aeronautics and  
Space Administration

Ames Research Center



Stanford University

JIAA TR-76

50380476

**EXPERIMENTAL STUDIES OF A DELTA WING  
WITH LEADING EDGE FLAPS**

(NASA-CR-181204) EXPERIMENTAL STUDIES OF A  
DELTA WING WITH LEADING EDGE FLAPS  
(Stanford Univ.) 40 p

N90-70569

Unclass

00/05 0098944

BY

CHYANG S. LEE

STANFORD UNIVERSITY  
DEPARTMENT OF AERONAUTICS AND ASTRONAUTICS

APRIL 1987

JIAA TR-76

EXPERIMENTAL STUDIES OF A DELTA WING  
WITH LEADING EDGE FLAPS

BY

CHYANG S. LEE

STANFORD UNIVERSITY  
DEPARTMENT OF AERONAUTICS AND ASTRONAUTICS

APRIL 1987

JIAA TR-76

EXPERIMENTAL STUDIES OF A DELTA WING  
WITH LEADING EDGE FLAPS

BY

CHYANG S. LEE

STANFORD UNIVERSITY  
DEPARTMENT OF AERONAUTICS AND ASTRONAUTICS

APRIL 1987

## ABSTRACT

This report documents an experimental investigation of a delta wing with leading edge flaps. The experiments include detailed surface pressure distributions, surface oil flow patterns and flow visualization using smoke and laser light. The measurements were conducted for angles of attack ranging from  $5^\circ$  to  $45^\circ$  at flap deflections of  $0^\circ$ ,  $15^\circ$ ,  $30^\circ$ , and  $45^\circ$ .

The flow visualization studies show that there are two vortices, the leading edge vortex and the hinge vortex, at low angles of attack and high flap deflections. The two vortices merge into one large wing vortex at angle of attack near  $20^\circ$ . The vortices are unstable and oscillating between merge and separation for angles of attack from  $15^\circ$  to  $20^\circ$  and a flap angle of  $45^\circ$ .

The pressure measurements indicate the flap can increase lift-to-drag ratio and delay vortex burst, but the suction peak is reduced. When the flap is offset slightly from the hinge line, part of the suction loss on the main wing can be recovered with a reduction in the flap normal force. The gain on the wing is generally larger than the loss on the flap, therefore, there is a total gain on the overall wing loading. However, the magnitude of the gain is small.

The normal forces on the wing and the flap can be empirically decomposed for the cases of  $45^\circ$  flap angle. The correlation shows a stronger linear force dependence on the wing, and the non-linear vortical flow component is larger on the flap.

## NOMENCLATURE

$b$	wing semi-span
$c$	wing root chord
$C_D$	sectional drag coefficient
$C_L$	sectional lift coefficient
$C_N$	sectional normal force coefficient
$C_{NF}$	sectional normal force coefficient on the flap
$C_{NW}$	sectional normal force coefficient for the wing
$C_P$	surface pressure coefficient
$k$	flap-wing area ratio
$k_1, k_2, p$	correlation constant
$x, y$	longitudinal and spanwise coordinates
$\alpha$	angle of attack
$\delta$	flap deflection angle
$\epsilon$	half apex angle

*superscripts :*

$\overline{(\quad)}$  averaged sectional coefficient by assuming a quasi-conical flow

## 1. INTRODUCTION

The demand for improved maneuverability for aircraft has stimulated new interest in high angle of attack aerodynamics.<sup>1</sup> The speeds during such maneuvers are typically low, therefore, high lift coefficients are required under these conditions. While conventional low aspect ratio wings suffer from limited angle of attack envelope and poor lift derivatives, delta wings can eliminate most of these problems. This improvement relies on the strong vortices trapped above the wing which cause a low pressure region, thereby enhancing the lifting capability. Typically, a lift derivative better than  $2\pi$  and a stall angle of attack higher than  $20^\circ$  can be achieved by a slender, sharp leading edge delta wing. Delta wings also have their limitations, such as vortex breakdown (limiting the maximum angle of attack), unsteady asymmetric vortex shedding (causing wing rock), and high drag (lowering lift-to-drag ratio). Extensive attempts have been made to alleviate some of these limitations through proper control of the wing vortices. Among them are tangential leading edge blowing to increase angle of attack envelope<sup>2</sup> and the use of leading edge vortex flaps to improve lift-to-drag ratio<sup>1</sup>.

Leading edge vortex flaps reduce drag on slender delta wings by controlling the vortex suction on the forward facing flap upper surfaces. A thrust component is produced on the flap and, therefore, drag decreases. A number of studies have been reported on this concept, both experimentally<sup>3</sup> and numerically<sup>4</sup>. These investigations showed that a deflected leading edge flap is capable of improving lift-to-drag ratio, but the strength of the wing vortex is reduced, hence it has a detrimental effect on lift characteristics. Since most of the previous experiments were conducted on generic wing-body or aircraft configurations, very limited data exists for simple geometries such as plain delta wings with straight flaps.

The objective of this study is to provide an experimental data base for a 'clean'

slender delta wing with leading edge flaps, which is essential for validating various numerical simulations, and to establish a fundamental understanding of the vortex structure of the flow field. This report documents the experimental results which include surface oil flow patterns, flow visualization using smoke and laser sheet, detailed surface pressure distributions and integrated aerodynamic coefficients.

The important parameters in this flow field, as shown in Fig. 1., are: angle of attack  $\alpha$ , flap deflection angle  $\delta$ , half apex angle of the wing  $\epsilon$ , spanwise length ratio (*i.e.* area ratio) of the flaps and the wing  $k$ , Reynolds number, and Mach number. In this investigation, only the effect of angle of attack and flap deflection are studied at low speed, all the other parameters are fixed.

## 2. APPARATUS

The experiments were performed in the 18×18-inch test section of the Stanford Low Speed Wind Tunnel. The free stream velocity was set at 20 m/s for the surface pressure measurements. The velocity was obtained by a reference static pressure difference from two stations in the contraction which has been shown to be free of model interference.

The delta wing has flat surfaces with sharp leading edges to simplify the model fabrication and the comparison of test results with conical flow predictions. The model is a 22° half apex angle (*i.e.* 68° sweep angle), 8-inch chord and 0.25-in constant thickness delta wing with conical leading edge flaps of 38.5% total wing area. Reynolds number based on free stream velocity of 20 m/s and the chord was  $0.3 \times 10^6$ . There are 174 pressure tappings distributed in six rows for measuring the spanwise pressure distributions at different chordwise locations. The model and the locations of pressure tappings are illustrated in Fig. 2. The relatively large flap

area is required to accommodate enough tapings on the flap for detailed resolution of the surface pressures, especially near the apex where the flow is expected to be near conical at high angles of attack. The model was mounted on a sting which can be rotated to adjust the angle of attack.

The surface pressures were measured by a 4 barrel, 48 port Scanivalve system which was integrated with a PDP-11/23 minicomputer. The pressure transducers were calibrated each time measurements were made. On-line data reduction and graphical display ensured the quality of measurements before the data were stored. The pressure measurements were conducted for angles of attack ranging from  $5^\circ$  to  $45^\circ$  at flap deflections of  $0^\circ$ ,  $15^\circ$ ,  $30^\circ$ , and  $45^\circ$ .

A second similar model, equipped with internal tubes for smoke ejection, was fabricated for the smoke-laser sheet flow visualization. This model was also used for the surface oil flow studies.

### 3. FLOW VISUALIZATION

#### 3.1 Surface Oil Flow

Titanium dioxide mixed with light mineral oil was painted on the model for the surface oil flow experiments. The model was tested for three minutes at the free stream velocity of 20 m/s before still photographs were taken. Figs. 3 and 4 show the sketches of typical streamline patterns obtained by this method. The associated flow fields in the cross plane are also presented in the same figures.

At  $\alpha = 5^\circ$  and  $\delta = 0^\circ$ , there is a large region of nearly parallel flow around the central line, showing the flow is mostly attached. The flow separates from the sharp leading edge forming a vortex. The air drawn by this vortex moves the streamline



sideways near the leading edge. The thick deposit of oil between these two region indicates the reattachment line of the vortex. When the flaps are deflected  $45^\circ$ , the streamline pattern becomes more complicated, as shown in Fig 3-b. The noticeable changes are : 1.) the reattachment line moves outboard and 2.) the streamlines near the leading edge cease to align with the cross flow. These indicate the leading edge vortex becomes weaker and smaller. The flap deflection also reduces the streamwise attached flow near the center. A large but weak (judging from the slope of the surface streamlines) hinge vortex occupies most of the space on the wing. The second line of oil deposit, corresponding to the separation line of the hinge vortex, coincides with the flap hinge.

At  $\alpha = 20^\circ$  and  $\delta = 0^\circ$ , as shown in Fig. 4-a, the streamline pattern is typical for delta wings at high angle of attack. The herring bone type of streamline on the wing is the trace of the wing vortex. The large suction from the vortex produces a strong adverse pressure gradient between the core and the leading edge. A secondary vortex sheet springs from there and forms a secondary separation line. The secondary vortex rotates in the opposite direction to the main vortex and, therefore, the slopes of the streamlines for the main and secondary vortices have different signs. The secondary vortex originates from a viscous interaction between the boundary layer on the wing upper surface and the potential field of the wing vortex, hence the position and strength of the secondary vortex will depend on the Reynolds number.

When the flap is deflected  $45^\circ$  at  $\alpha = 20^\circ$ , as shown in Fig. 4-b, the secondary separation line moves toward the leading edge. The streamwise attached flow and the reattachment line of the wing vortex reappear on the wing, indicating that the vortices have become smaller and moved closer to the leading edge. Although the separation and reattachment lines remain straight on the wing surface at  $\alpha = 20^\circ$ ,

this does not necessarily imply that the flow field is conical. The variation of the slopes on the main vortex traces for  $\alpha = 20^\circ$  and  $\delta = 0^\circ$  reveals that the trailing edge effect is not negligible in this case. This observation is consistent with the chordwise loading variation that will be discussed later.

### 3.2 Smoke Flow Visualization

The smoke flow visualization model, which has ten small holes along the leading edge for ejecting the smoke, is the same size as the pressure tapping model. A simple smoke generator was built from a cylindrical container. Incense was burnt in the container and the airflow through the chamber was adjustable to obtain the optimal smoke quality. However, the flow rate was kept relatively low to minimize the disturbance to the flow field. A one-watt argon laser was used as the light source. The light was directed through a set of optical mirrors mounted on a traversing gear which permitted the projection of the light sheet at various locations in the streamwise direction. Experience showed that the smoke diffused too fast to obtain clear images at 20 m/s. Therefore, the free stream velocity was set at around 10 m/s for the smoke flow experiments. The flow visualization was recorded on a video tape and still photographs were taken from the frozen video frames. The figures shown are sketches duplicated from the still photos.

The patterns of wing vortices for a flap deflection of  $45^\circ$  and different angles of attack are presented in Fig. 5. The leading edge vortex is located on the flap surface for angles of attack between  $5^\circ$  and  $15^\circ$  and the size of the leading edge vortex increases with angle of attack. There is a salient vortex arising from the flap hinge over this range of angles of attack. The size of this hinge vortex increases with  $\alpha$ , and its location moves toward the hinge line as  $\alpha$  increases. The size of the hinge vortex is always larger than the leading edge vortex, but there is no parallel

comparison that can be made on its strength. At  $\alpha = 20^\circ$ , these two vortices merge into one. For angles of attack larger than  $25^\circ$ , the flow becomes unstable and leaves the wing surfaces, indicating vortex burst at that location.

Further examination of the flow visualization record showed that the merge of the leading edge vortex and hinge vortex is a very unstable process. The merge does not occur at a fixed angle of attack, but over the range of  $15^\circ < \alpha < 20^\circ$  for  $\delta = 45^\circ$ . Even at a fixed angle of attack in this range, the vortices can flip-flop between merge and separation. At  $\alpha = 15^\circ$ , a small hinge vortex sits on the wing while a larger vortex springs from the leading edge as shown in Fig. 6-a. The leading edge vortex is drawn toward the wing surface and merges with the hinge vortex as in Fig. 6-b. A similar situation occurs at  $\alpha = 20^\circ$ , separate leading edge and hinge vortices are illustrated in Fig. 7-a, and Fig. 7-b shows the vortex after merging.

The unstable leading edge and hinge vortices may cause fluctuations in rolling moment at some 'critical angles of attack'. It is believed that the unstable merging is a viscous interaction between the two closely spaced vortices of the same sign. Therefore, this critical angle should be a function of Reynolds number, free stream disturbance and geometric parameters (e.g.  $\epsilon, \delta, k$ ). However, more study is needed before a conclusion can be reached about this phenomenon.

## 4. SURFACE PRESSURE MEASUREMENTS

### 4.1 Surface Pressure Distribution

Spanwise pressure distributions at  $x/c = 0.375$  are presented in Figs. 8-a through 8-h for different angles of attack and flap deflections. In each plot, the effect of flap deflection is shown for constant angle of attack. In general, the pres-

sure distribution exhibits a suction peak produced by the strong wing vortex near the hinge line and, close to the leading edge, there is a plateau generated by the secondary vortex as discussed in the surface oil flow patterns. At a fixed angle of attack, the flap deflection decreases the wing suction peak and this reduction increases with the flap deflection angle. At low angles of attack, two suction peaks corresponding to the separate leading edge and hinge vortices can be observed as shown in Fig. 8-a for  $\alpha = 5^\circ$ . The hinge vortex always generates lower suction than the leading edge vortex. When the angle of attack is higher than  $15^\circ$ , only one suction peak is observed. This measurement is time averaged, hence it cannot detect unsteadiness in surface pressure at the corresponding critical angles of attack observed in the smoke flow visualization. However, this may indicate that the separation of the leading edge and hinge vortices is an unstable state. The two vortex system can only exist temporarily, therefore, the time averaged pressure distribution shows only one suction peak. In Fig. 8-e, at  $\alpha = 25^\circ$ , for  $\delta = 15^\circ$  and  $\delta = 30^\circ$ , the suction peak is almost the same as that with no flap deflection, which shows that for certain combinations of  $\alpha$  and  $\delta$ , the main effect of flap deflection is to displace the suction toward the leading edge. When  $\alpha$  is higher than  $35^\circ$ , the suction peak on the plain delta wing decreases with angle of attack, while the suction persists to much higher angles of attack when the flap is deflected. Fig. 8-h shows the suction peak is completely removed for the plain wing at  $\alpha = 40^\circ$ , but a strong suction still exists when the flap is deflected. This illustrates the effect of leading edge flaps in delaying the vortex burst.

## 4.2 Force Coefficients

The sectional normal force coefficient can be obtained from integrating the

surface pressure over the individual spanwise rows,

$$C_N = \oint C_P d\left(\frac{y}{b}\right). \quad (1)$$

This integration is performed separately for the main wing ( $C_{NW}$ ) and flap ( $C_{NF}$ ). The chordwise normal force coefficients for the main wing and flap are presented in Figs. 9 and 10. The integrated value at the first row,  $x/c = 0.25$ , is not shown in the figures due to the error introduced by the lack of sufficient pressure tapings.

Both  $C_{NW}$  and  $C_{NF}$  decrease when the flap is deflected. In a conical flow,  $C_{NW}$  and  $C_{NF}$  should be constant along the chord. This is approximately true at low angles of attack. At high angles of attack,  $\alpha > 15^\circ$ , the Kutta condition demands zero loading at the trailing edge, therefore, for the those conditions, the loading decreases along the chord. At  $\alpha = 5^\circ$ , the loading increases along the chord, which is opposite to the trailing edge effect. This can be attributed to the constant thickness of the model, which produces a larger effective thickness in the conical plane near the apex and results in a departure from conicality.

To simplify the analysis of the chordwise loading variations, an averaged normal force coefficient is determined by assuming a quasi-conical flow as

$$\bar{C}_N = \frac{\int C_N \cdot b dx}{\int b dx}. \quad (2)$$

The effect of flap deflection on the averaged normal force coefficients is presented in Fig. 11. The change of the normal force on the main wing is independent of the flap deflection angle over a wide range of angle of attack,  $20^\circ < \alpha < 35^\circ$ . However, the decrement of the normal force on the flap increases with the flap angle.

The angle of attack at which the maximum flap normal force is produced increases with the flap deflection, this is due to the fact that the flap can preserve the suction peak at higher angle of attack as previously discussed.

The lift and drag components can be derived from the normal forces on the wing and flap. Through a coordinate transformation, the normal vector on the wing and flap can be expressed as a function of  $\alpha$ ,  $\delta$ , and  $\epsilon$ . The resultant lift and drag then can be obtained from the measured normal force components on the wing and flap as

$$\begin{aligned}\overline{C}_L &= \cos \alpha \left( \overline{C}_{NW} + \overline{C}_{NF} \cos \delta (1 + \sin \epsilon \tan \alpha \tan \delta) \right), \\ \overline{C}_D &= \sin \alpha \left( \overline{C}_{NW} + \overline{C}_{NF} \cos \delta \left( 1 - \frac{\sin \epsilon \tan \delta}{\tan \alpha} \right) \right).\end{aligned}\tag{3}$$

Fig. 12 shows the variation of  $\overline{C}_L$  and  $\overline{C}_D$  for different combinations of  $\alpha$  and  $\delta$ . Both lift and drag decrease with the flap deflection. For a flap deflection of  $45^\circ$ , the maximum angle of attack, before stall, increases from  $25^\circ$  to  $35^\circ$ .

The effect of leading edge flaps on lift-to-drag ratio is shown in Fig. 13-a as a function of  $\alpha$  and  $\delta$ . At a fixed angle of attack, the deflected flap increases L/D, but the lift is reduced due to the weakening of the wing vortex. This can be illustrated more clearly by a cross plot of  $\overline{C}_L/\overline{C}_D$  against  $\overline{C}_L$  as shown in Fig. 13-b. In general, for a flapped wing, the required angle of attack to produce a fixed value of  $\overline{C}_L$  is higher, and the corresponding  $\overline{C}_L/\overline{C}_D$  is lower. However, at low angles of attack,  $\alpha < 10^\circ$ , the flapped wing has higher  $\overline{C}_L$  and  $\overline{C}_L/\overline{C}_D$  values.

### 4.3 Slotted Flap

To improve the lift characteristics of the vortex flap, measurements were made with the flap offset 1/16-in. from the hinge line at the trailing edge. The purpose

of the slotted flap is to energize the vortex near the wing-flap junction by the flow through the slot. The suction on the flap is expected to be lower than that of a normal flap without a slot, since less mass will separate at the leading edge. This can be understood by the fact that the main wing has an attached flow region near the center, therefore, a small amount of mass injection through the slot should be able to cause the flow to separate and produce suction on the main wing. By this argument, the size of the slot should be of the order of the local boundary layer thickness to minimize the loss of suction on the flap.

Typical spanwise pressure distributions at mid-chord for  $\alpha = 25^\circ$  with different flap settings are presented in Fig. 14. The slotted flap can recover some of the suction loss on the main wing, but it also has suction loss outboard of the maximum suction point. Fig. 15 shows the integrated normal force coefficients for  $\delta = 45^\circ$ . With the slot, the loss of normal force on the main wing can be recovered by nearly 50% for angles of attack ranging from  $20^\circ$  to  $30^\circ$ . The reduction of the force coefficient on the flap is expected, and it is about half of the gain on the main wing. Therefore, there is a net gain on the overall wing loading through the use of the slot. The change on the lift and drag coefficients is shown in Fig. 16.  $\overline{C}_L$  increases with the slotted flap for  $15^\circ < \alpha < 35^\circ$ , but the magnitude is less impressive than the gain in the wing normal force. Due to the reduction of the flap normal force, the drag also increases with the slotted flap.

#### 4.4 Correlation of Sectional Normal Force Coefficient

The variation of normal force as a function of angle of attack for a delta wing in conical flow can be approximated by the following expression,<sup>5</sup>

$$\frac{C_N}{(b/c)^2} = 2\pi k_1 \frac{\alpha}{b/c} + k_2 \left( \frac{\alpha}{b/c} \right)^p \quad (4)$$

where  $k_1$ ,  $k_2$ , and  $p$  are constants depending upon the wing geometry. The first

linear term represents the contribution from R. T. Jones' attached flow calculation, the second non-linear term comes from the force induced by the wing vortex. The constants had been calculated by Smith<sup>6</sup> as  $k_1 = 1.0$ ,  $k_2 = 4.9$ , and  $p = 1.7$  for a slender, thin delta wing, and these compare well with other measurements at low speed.

Since the flow parameters are closer to conical and less affected by the trailing edge near the apex, the normal force coefficients at  $x/c = 0.375$  in this experiment are checked against Eq. 4 for the cases without flap deflection. The constant  $k_1$  represents a weighting parameter of the linear force, and it can be determined from the measured data. The non-linear component should be vanished at  $\alpha = 0^\circ$  when the flow is fully attached, therefore,

$$k_1 = \frac{1}{2\pi b/c} \left( \frac{C_N}{\alpha} \right)_{\alpha=0} \quad (5)$$

where  $b/c = 0.406$  for the present model. The value of  $k_1$  was approximated by differentiating a spline curve fit of  $C_N$  and  $\alpha$  in the range of  $0^\circ < \alpha < 15^\circ$ . After  $k_1$  is determined, the value of  $k_2$  and  $p$  can be obtained through linear regression by taking the logarithm of both sides of the equation. The correlated constants are within 5% of Smith's calculation as shown in Table 1, which indicates the flow is conical at this chordwise location. Fig. 17-a illustrates that good agreement can be found up to  $\alpha = 25^\circ$ .

The normal force on the flapped wing is also correlated using the same method. The corresponding aspect ratio and normal force coefficient are

$$\begin{aligned} b/c &= (b/c)_{wing} + (b/c)_{flap} \cos \delta, \\ C_N &= C_{NW} + C_{NF} \cos \delta. \end{aligned} \quad (6)$$

For  $\delta = 45^\circ$ , the agreement between the correlation and the measured data is



reasonable as shown in Fig. 17-b. The values of correlation constants are also given in Table 1.

From the flow visualization study, there are separate leading edge and hinge vortices at low angles of attack. A reasonable conjecture is then to correlate  $C_{NW}$  and  $C_{NF}$  separately for the wing and the flap by Eq. 4. The corresponding  $b/c$  is 0.25 for the wing and 0.156 for the flap. When correlating the normal force on the flap, an effective angle of attack,  $\alpha_{eff} = \alpha \cos \delta$ , is used, since the flap is at an angle  $\delta$  relative to the main wing.

The resultant values for the flapped wing at  $\delta = 45^\circ$  are listed in Table 1, and the comparison of the correlation with measurements is shown in Fig. 18. The agreement of the correlation and the measured data is reasonable for  $C_{NW}$  at  $\alpha < 25^\circ$ , and for  $C_{NF}$  at  $\alpha < 20^\circ$ . This shows that the normal forces on the wing and the flap can be decomposed for  $\delta = 45^\circ$ . It is also possible to examine the ratio of the linear and non-linear forces acting on the wing and the flap. The constant  $k_1$  is larger for the main wing, indicating a larger linear attached flow influence, while for the flap, the non-linear vortical flow component is larger.

No parallel correlation can be found for  $\delta = 15^\circ$  and  $30^\circ$ . At low flap deflections, the hinge vortex is less likely to separate from the leading edge vortex, and this may make the assumption of loading decomposition invalid.

## 5. CONCLUDING REMARKS

An experimental study on a delta wing with leading edge flaps has been completed. The experiments include surface pressure measurements and flow visualization by surface oil flow and smoke-laser light sheet.

Distinct leading edge and hinge vortices exist only at low angles of attack and high flap angles. The two vortices merge into one wing vortex when the angle of attack is between  $15^\circ$  and  $20^\circ$  for a flap deflection of  $45^\circ$ . The merge is unstable and may cause fluctuation in rolling moment.

With no flap deflection, the sectional normal force coefficients at  $x/c = 0.375$  agree well with predicted values for angles of attack up to  $25^\circ$ , which indicates the flow is conical at this location. Therefore, the pressure distributions in the present measurements can be used as a data base for validating various conical flow calculations. For the flap deflection of  $45^\circ$ , the normal force on the wing and the flap can be decomposed by the proper slenderness ratio and effective angle of attack. No similar correlation can be found for  $\delta = 15^\circ$  and  $30^\circ$ .

## 6. REFERENCE

1. Lamar, J. E. and Campbell, J. F., "Vortex Flaps - Advanced Control Devices for Supercruise Fighters," Aerospace America, Jan. 1984.
2. Wood, N. J., and Roberts, L., "The Control of Vortical Lift on Delta Wings by Tangential Leading Edge Blowing," AIAA paper 87-0158.
3. Rao, D. M., "Vortical Flow Management for Improved Configuration Aerodynamics - Recent Experiences," AGARD CP-342.
4. Oh, S., and Tavella, D., "Analytical Observations on the Aerodynamics of a Delta Wing with Leading Edge Flaps," AIAA paper 86-1790.
5. Kuchmann, D., The Aerodynamic Design of Aircraft, Pergamon Press, 1979.
6. Smith, J. H. B., "Improved Calculations of Leading-Edge Separation from Slender, Thin, Delta Wings," RAE TR-66070, 1966.

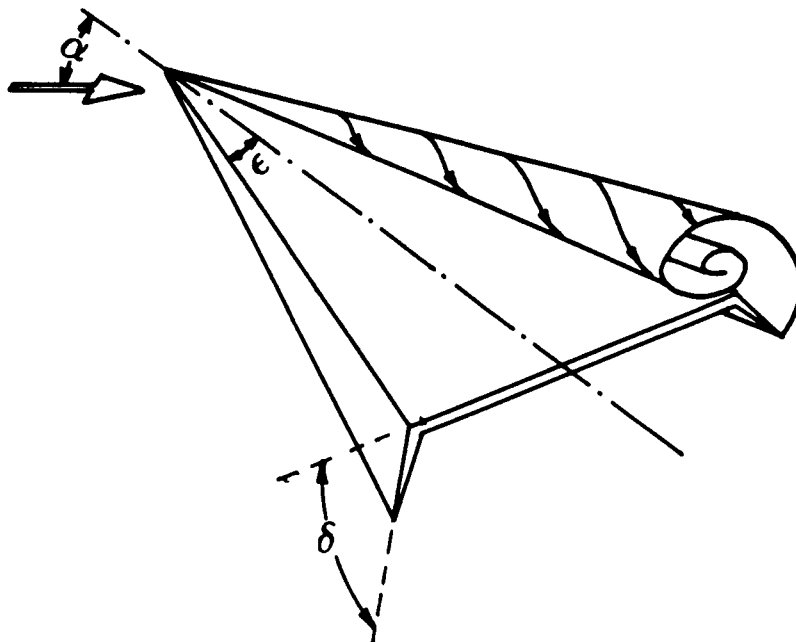


Fig. 1. Delta wing with leading edge flaps.

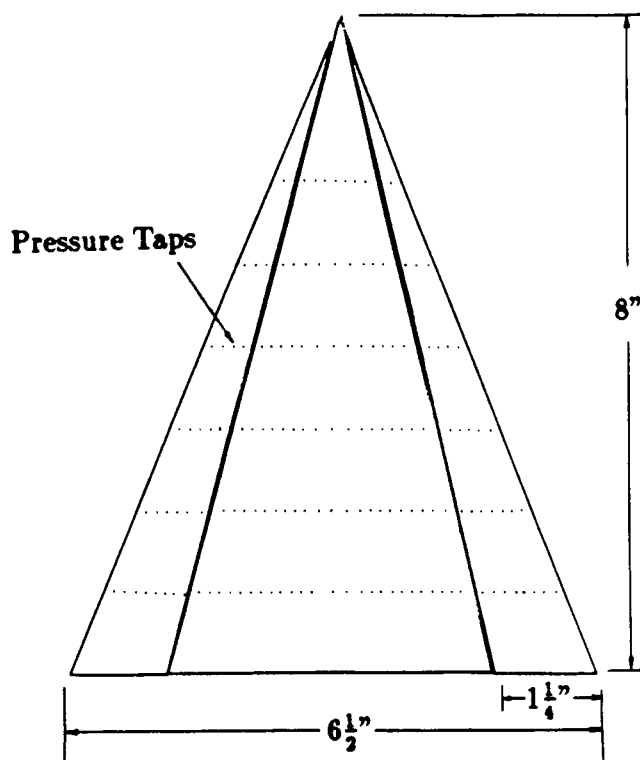
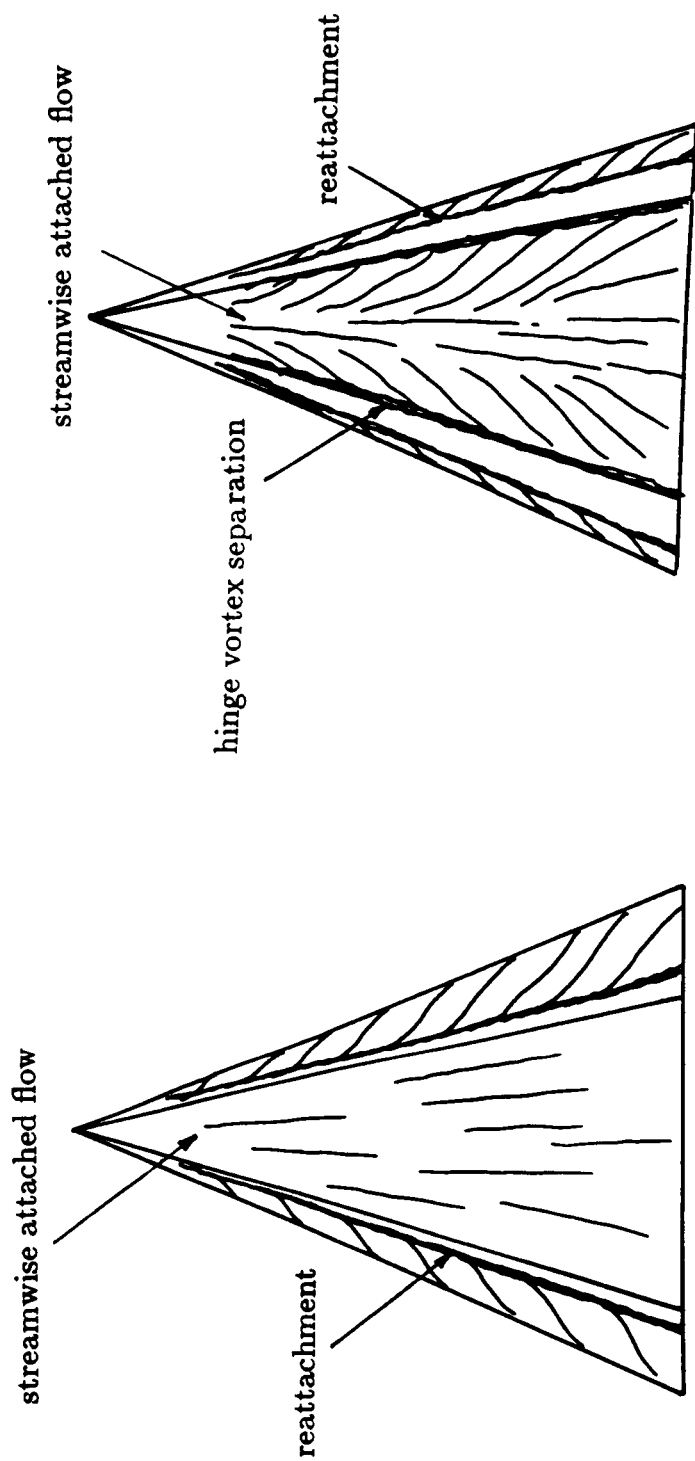


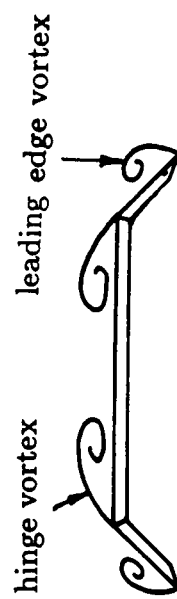
Fig. 2. The wind tunnel model.



leading edge vortex



(a)  $\alpha = 5^\circ, \delta = 0^\circ$



(b)  $\alpha = 5^\circ, \delta = 45^\circ$

Fig. 3. Surface oil flow patterns and the associated flow fields.

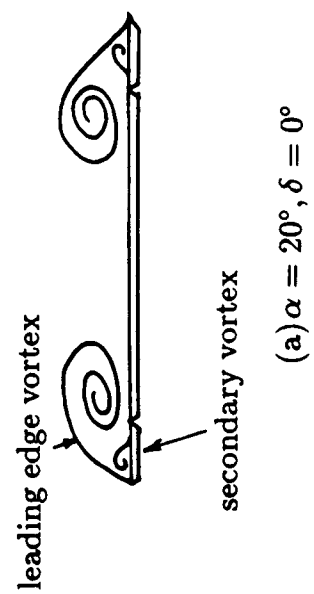
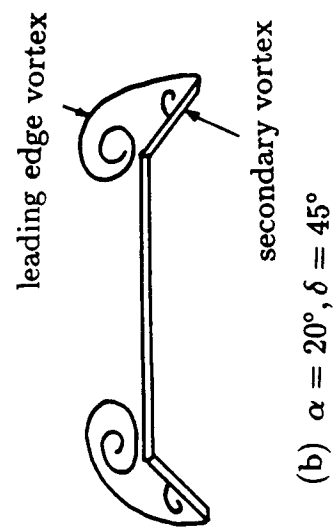
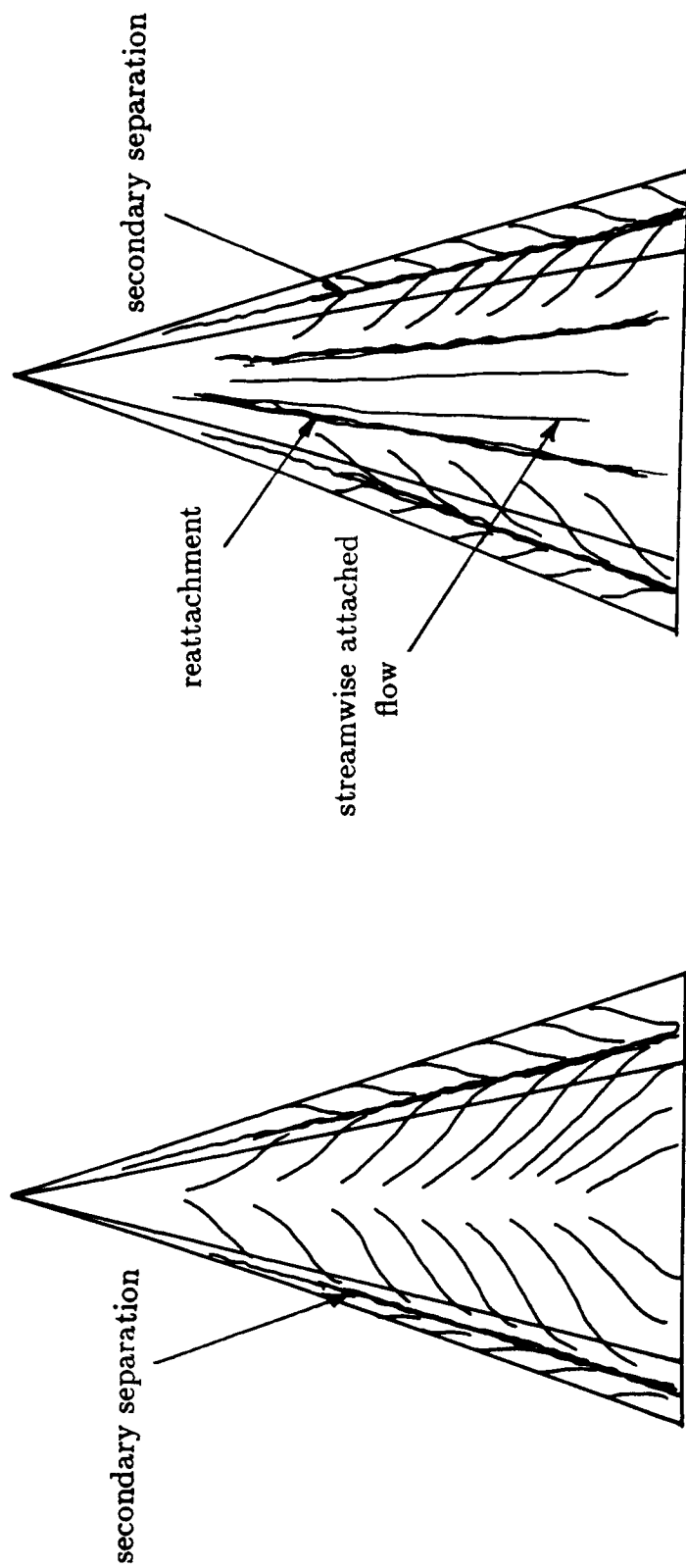
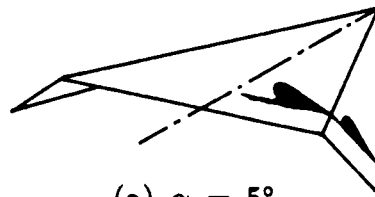
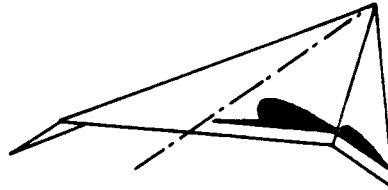


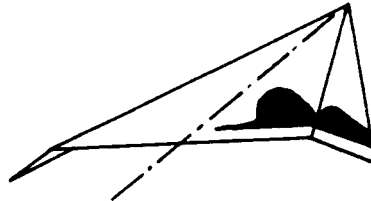
Fig. 4. Surface oil flow patterns and the associated flow fields.



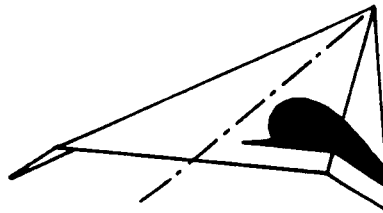
(a)  $\alpha = 5^\circ$



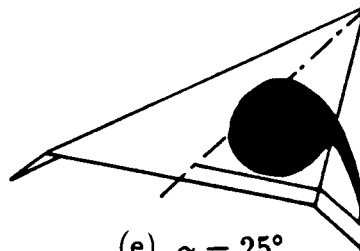
(b)  $\alpha = 10^\circ$



(c)  $\alpha = 15^\circ$



(d)  $\alpha = 20^\circ$



(e)  $\alpha = 25^\circ$

Fig. 5. The vortex patterns at  $\delta = 45^\circ$  and different angles of attack from the smoke flow visualization.

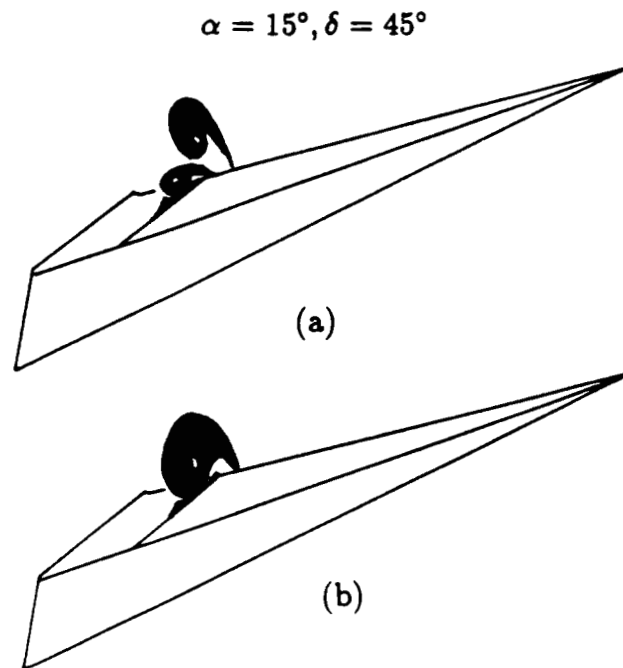


Fig. 6. Unstable merge and separation of the leading edge vortex and the hinge vortex,  $\alpha = 15^\circ, \delta = 45^\circ$ .

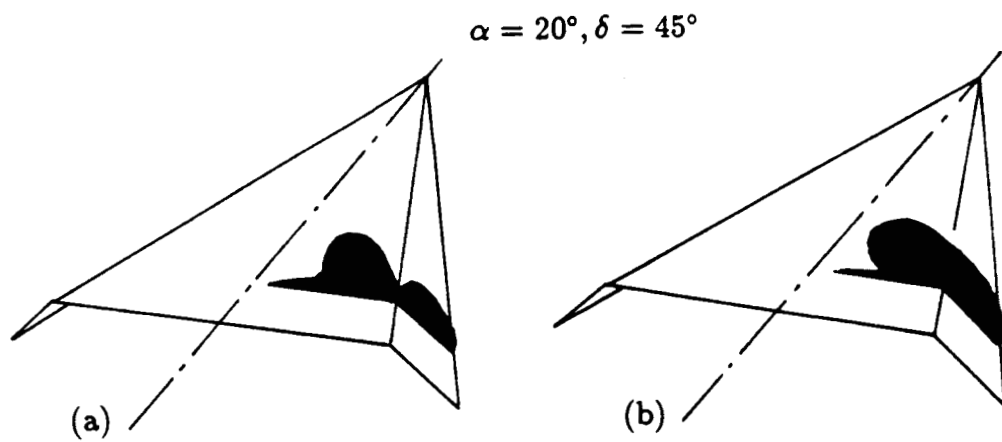
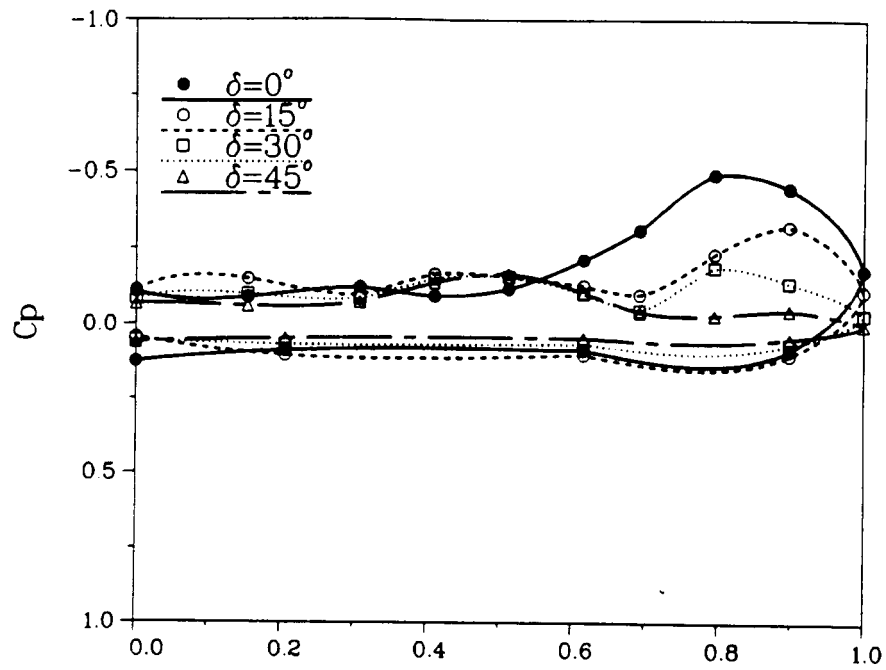


Fig. 7. Unstable merge and separation of the leading edge vortex and the hinge vortex,  $\alpha = 20^\circ, \delta = 45^\circ$ .

(a)  $\alpha=5^\circ$ ,  $x/c=0.375$



(b)  $\alpha=10^\circ$ ,  $x/c=0.375$

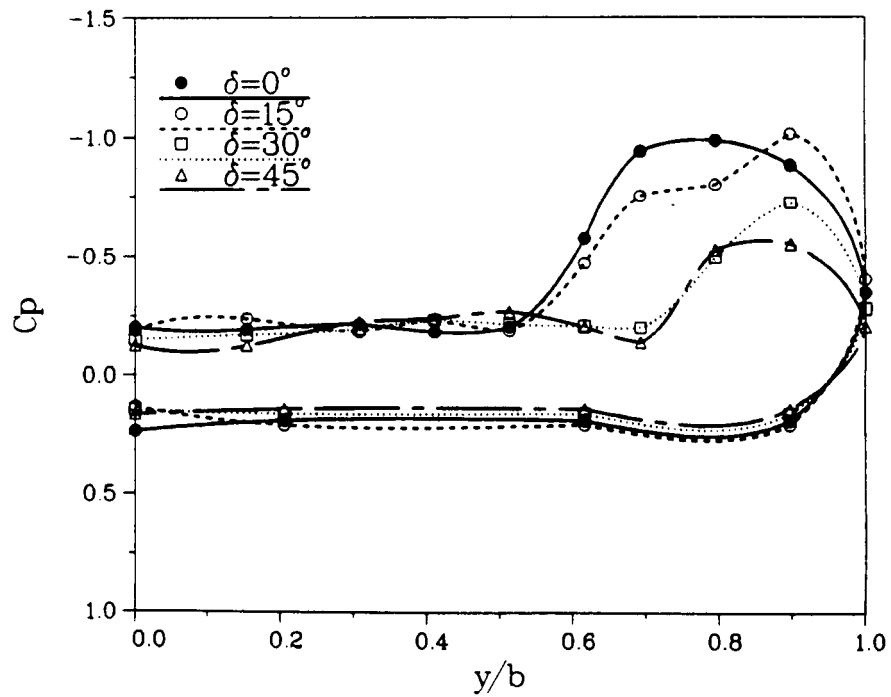
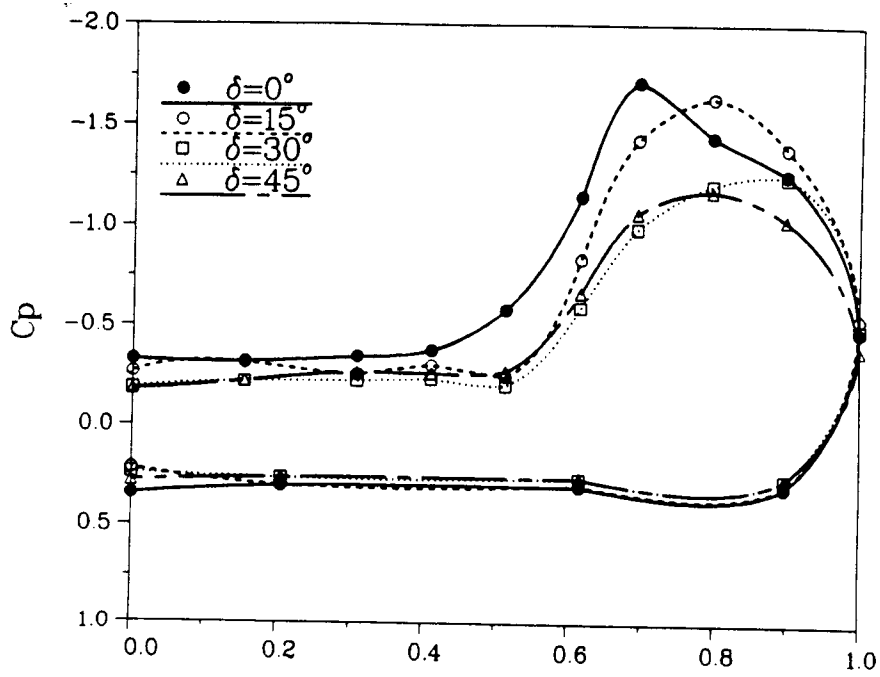


Fig. 8. Spanwise pressure distributions.



(c)  $\alpha=15^\circ$ ,  $x/c=0.375$



(d)  $\alpha=20^\circ$ ,  $x/c=0.375$

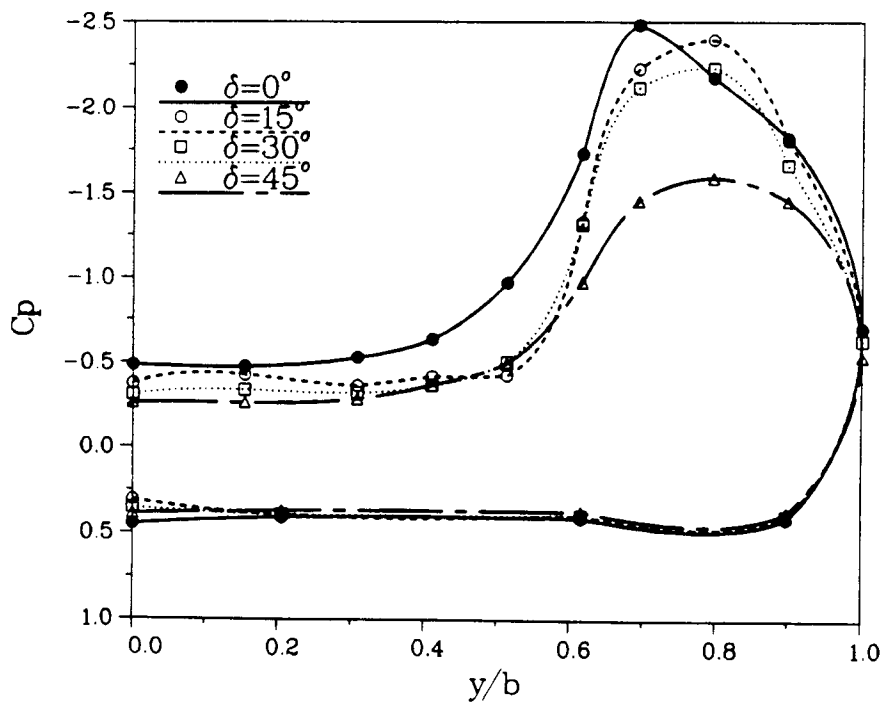
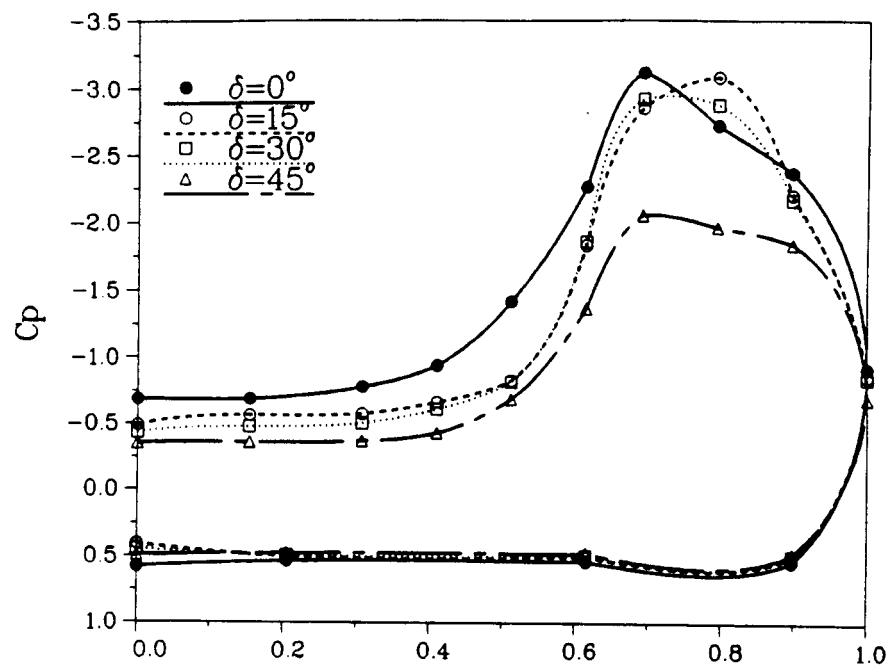


Fig. 8. Spanwise pressure distributions.

(e)  $\alpha=25^\circ$ ,  $x/c=0.375$



(f)  $\alpha=30^\circ$ ,  $x/c=0.375$

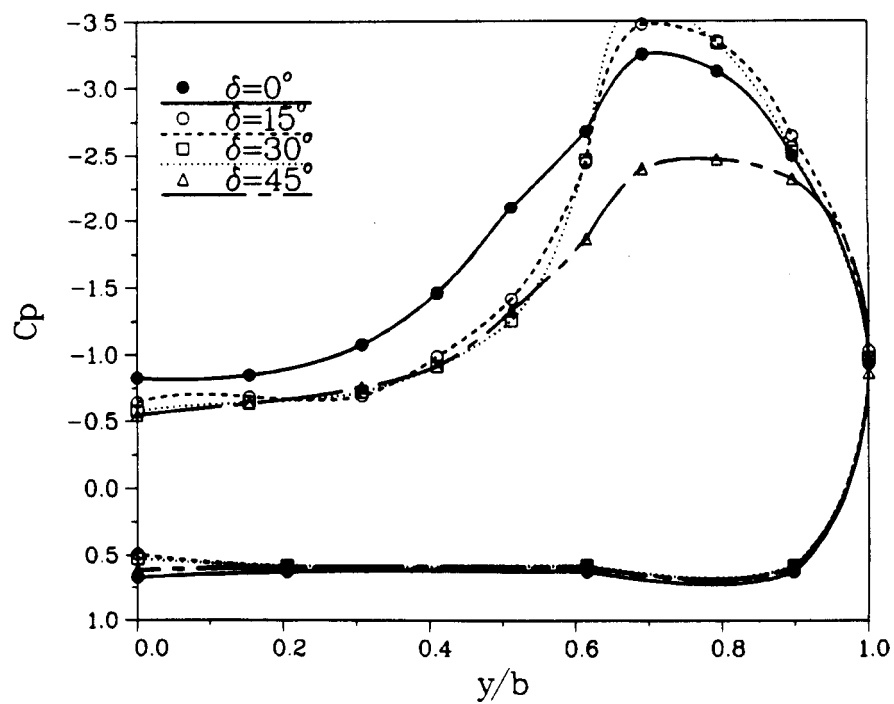
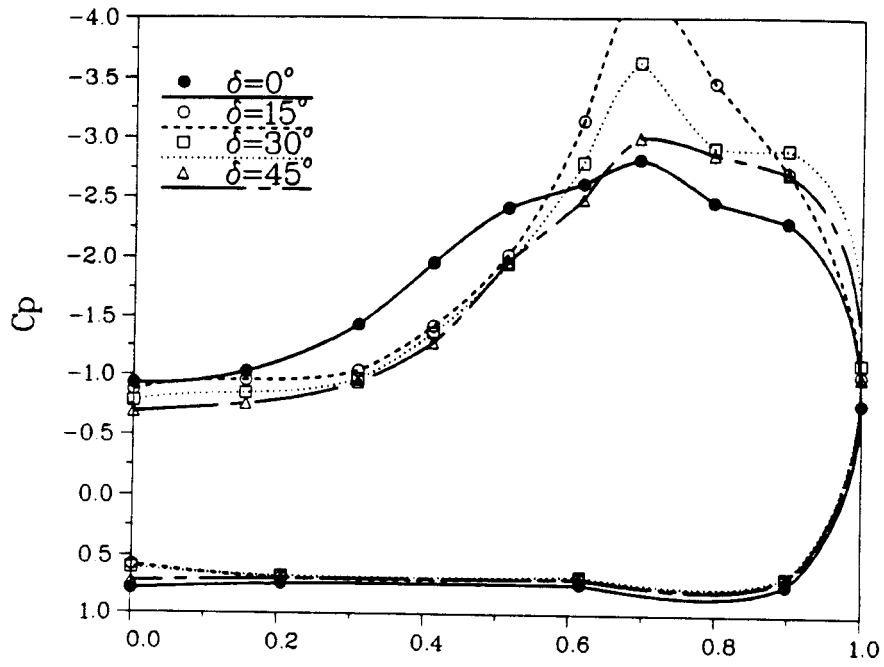


Fig. 8. Spanwise pressure distributions.

(g)  $\alpha=35^\circ$ ,  $x/c=0.375$



(h)  $\alpha=40^\circ$ ,  $x/c=0.375$

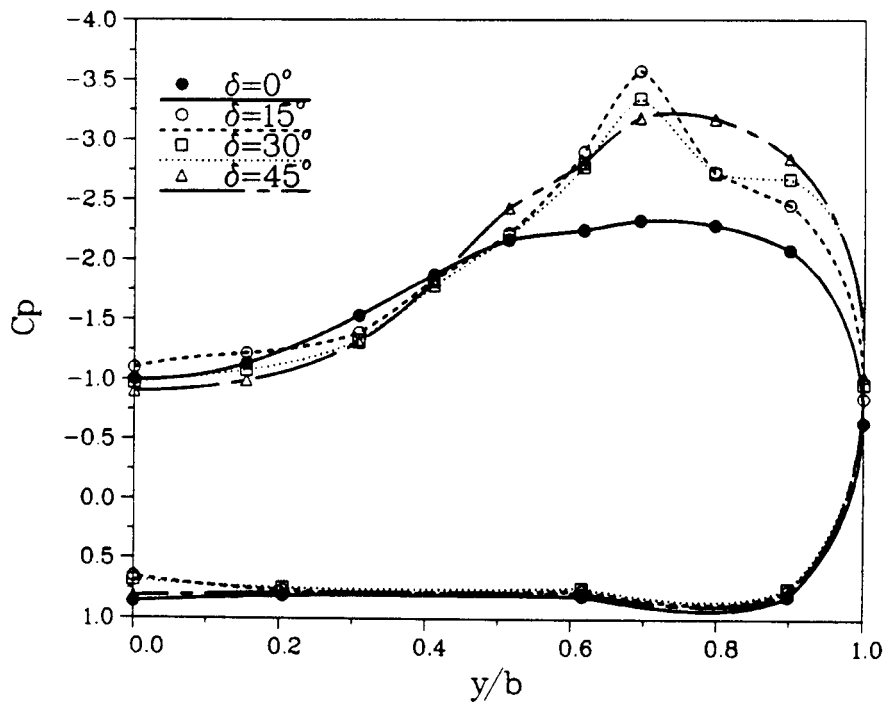


Fig. 8. Spanwise pressure distributions.

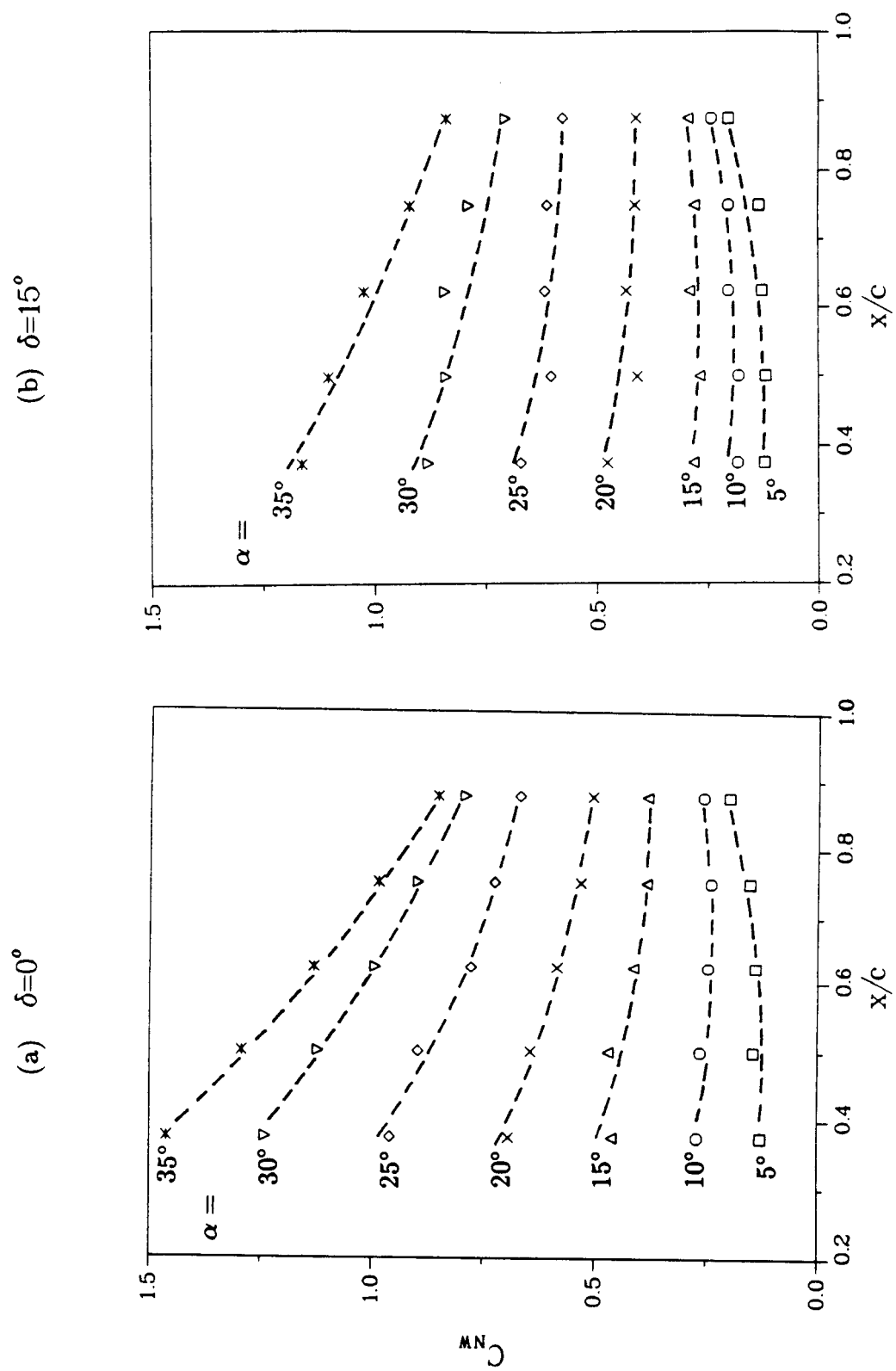


Fig. 9. Chordwise variation of the normal force coefficient on the wing.

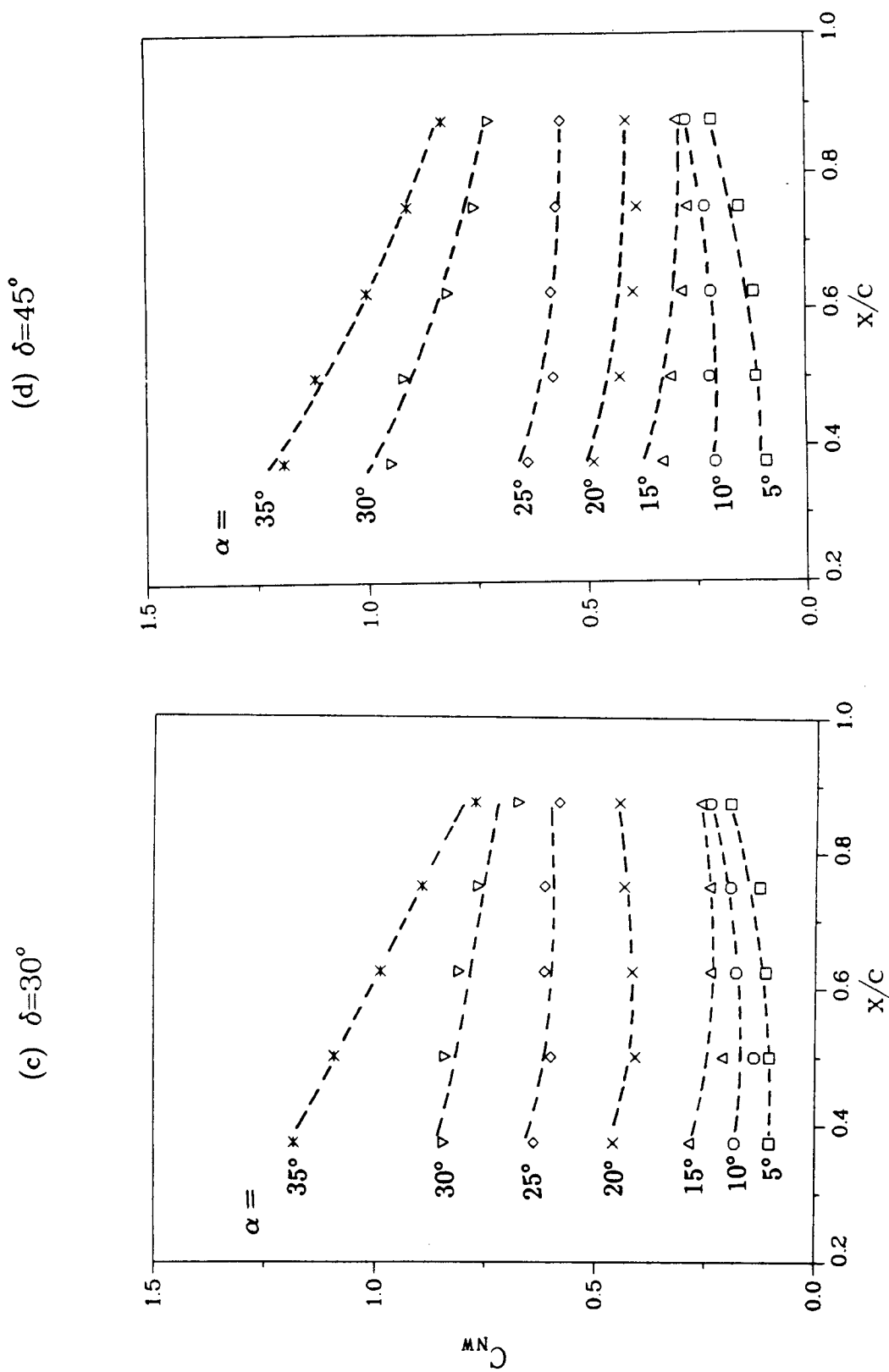


Fig. 9. Chordwise variation of the normal force coefficient on the wing.

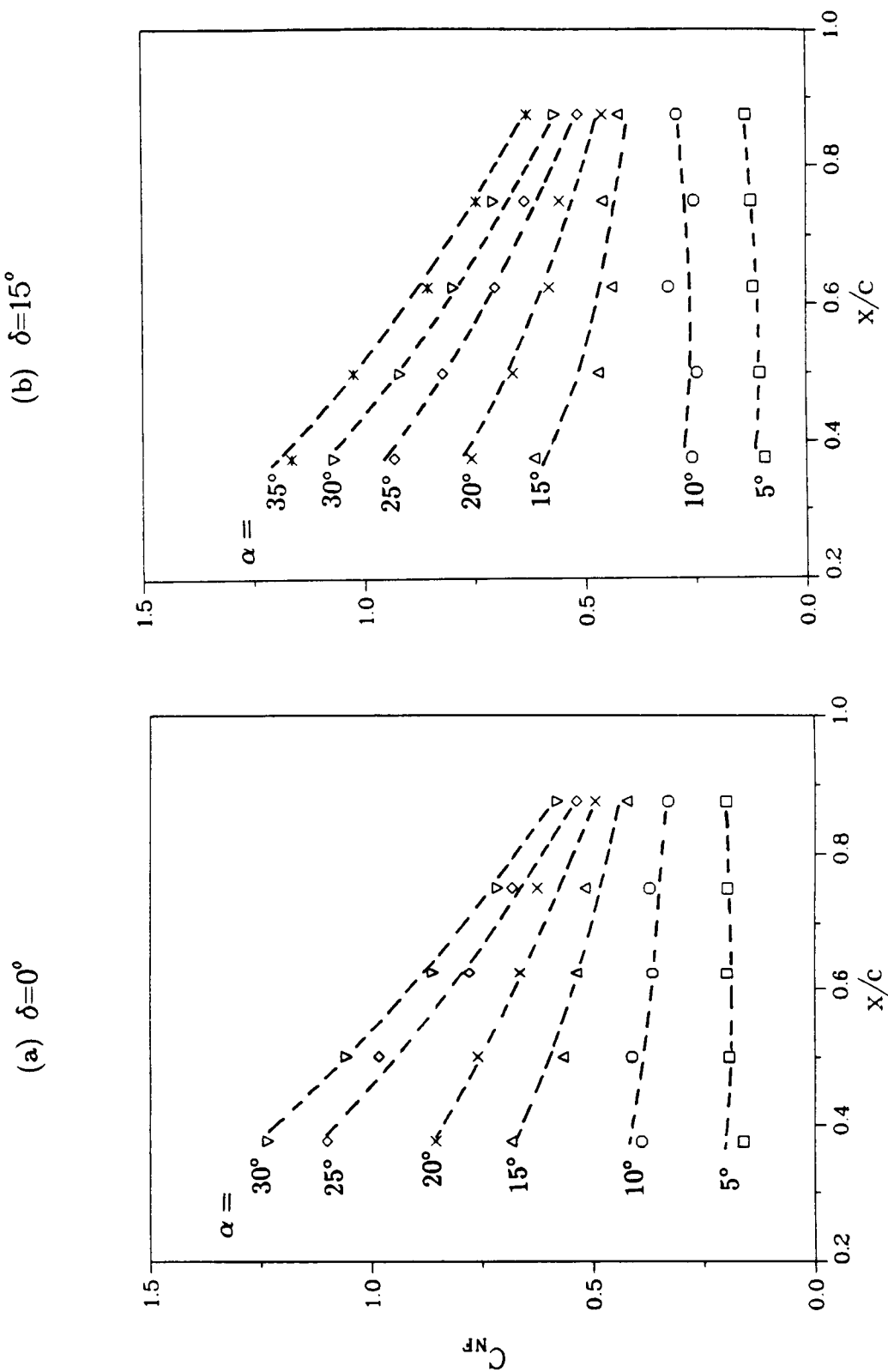
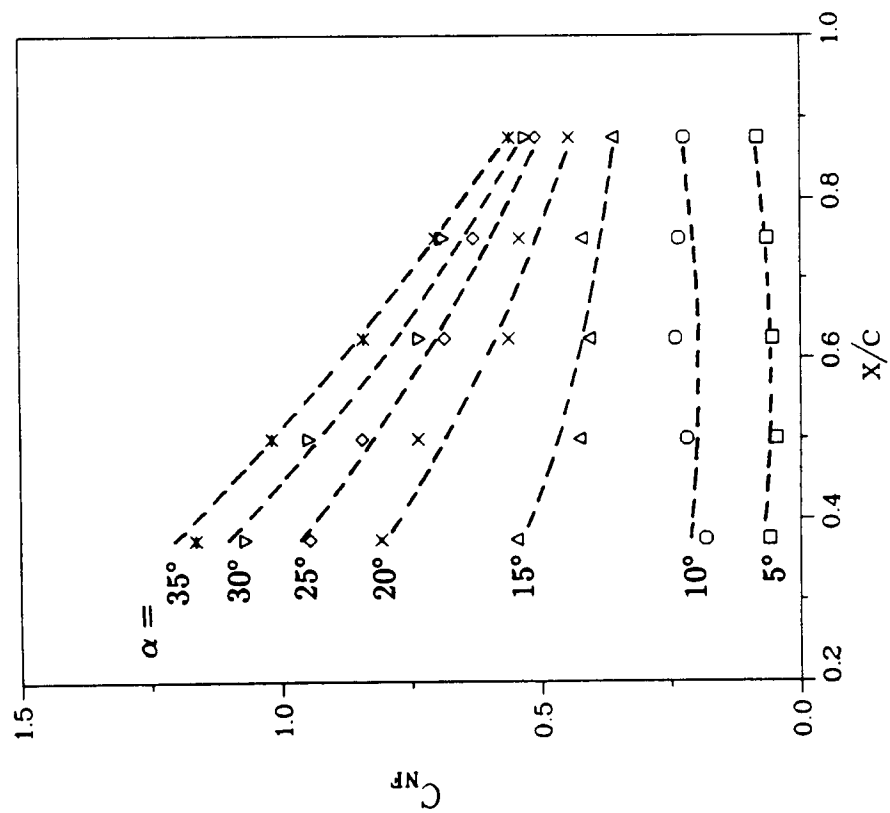


Fig. 10. Chordwise variation of the normal force coefficient on the flap.

(c)  $\delta=30^\circ$



(d)  $\delta=45^\circ$

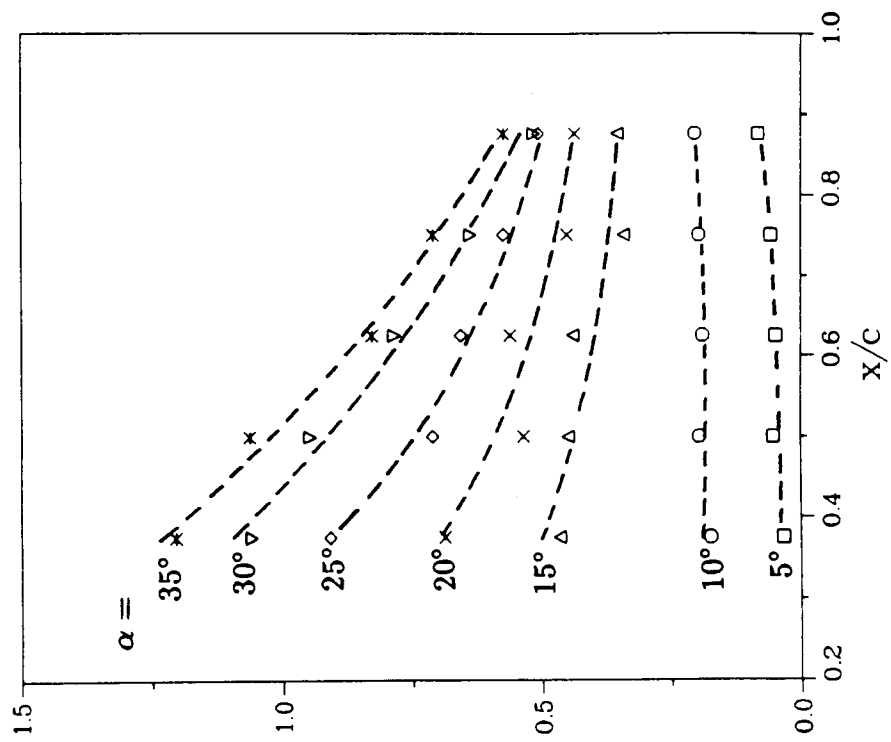


Fig. 10. Chordwise variation of the normal force coefficient on the flap.

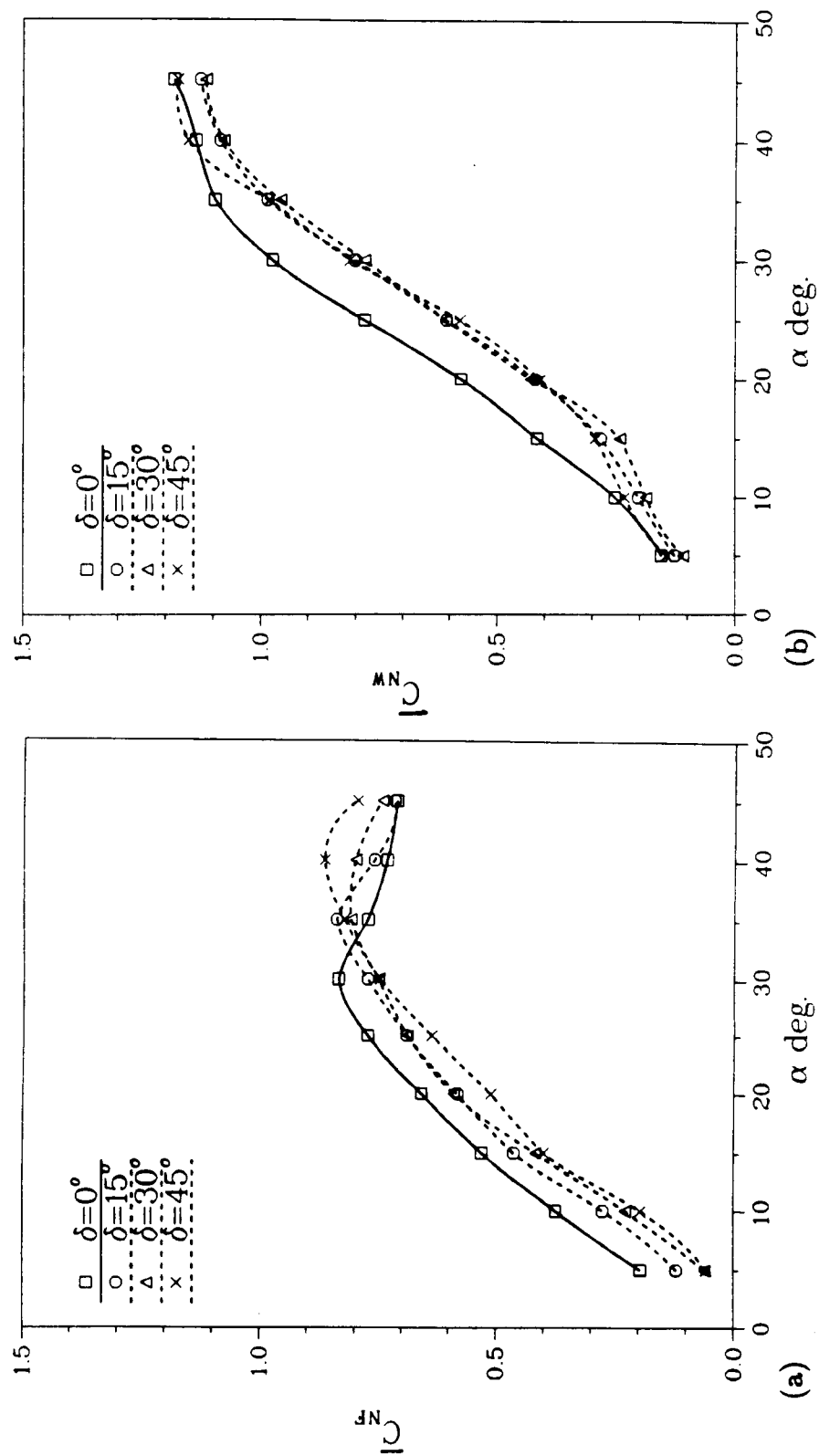


Fig. 11. Variation of averaged normal force coefficient.



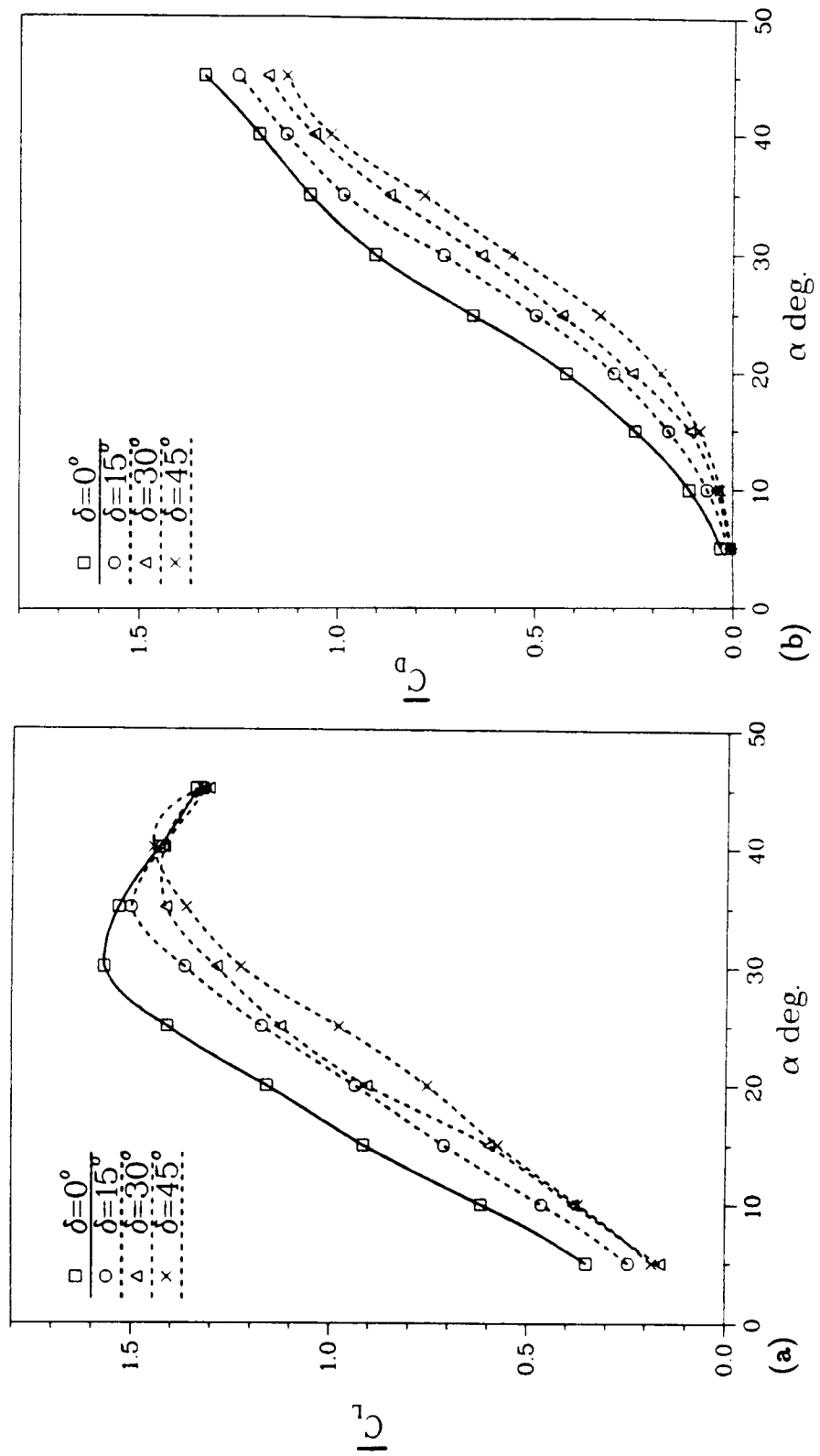


Fig. 12. Variation of averaged lift and drag coefficient.

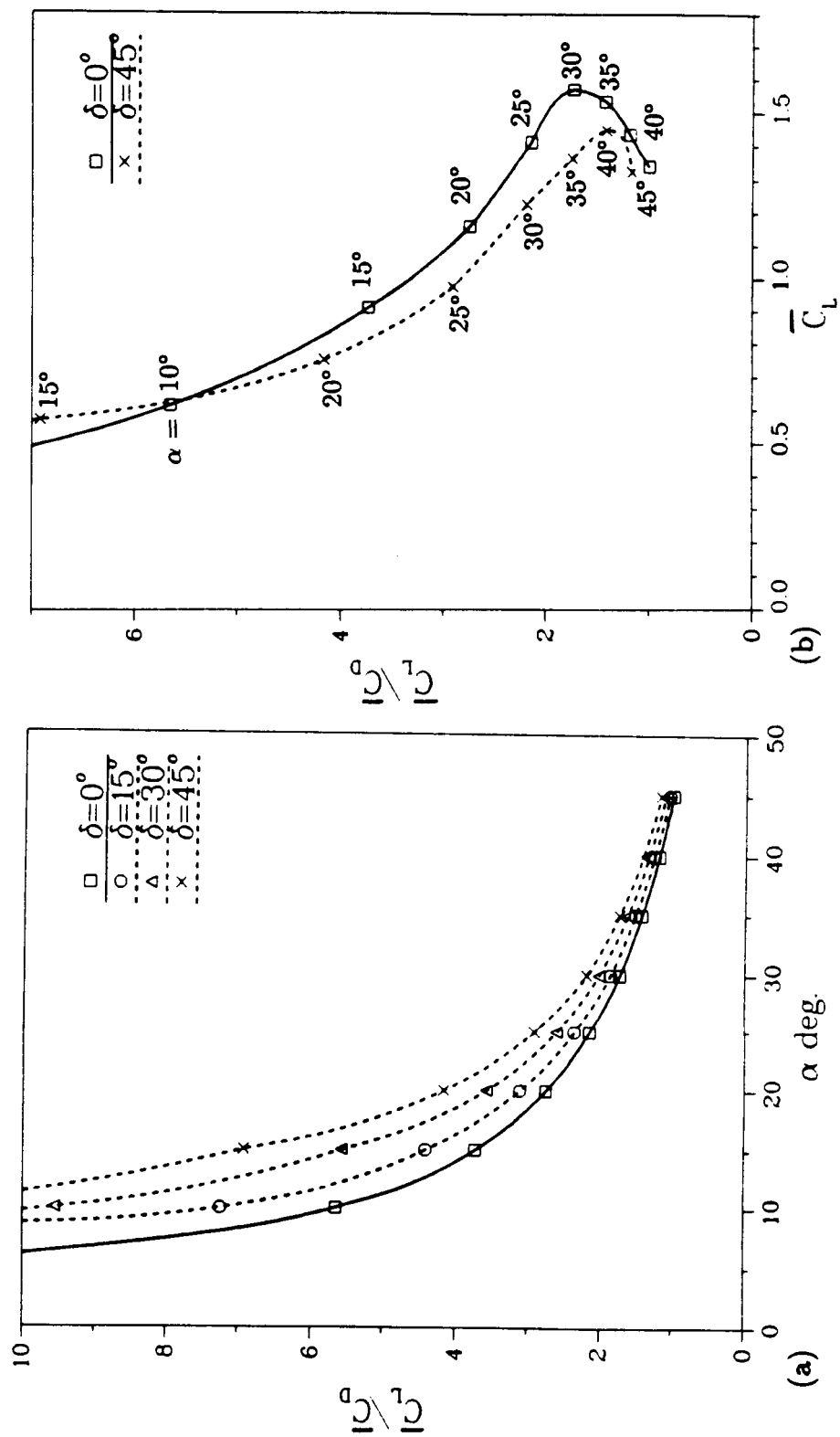


Fig. 13. Variation of averaged lift-to-drag ratio.

$\alpha=25^\circ, x/c=0.5$

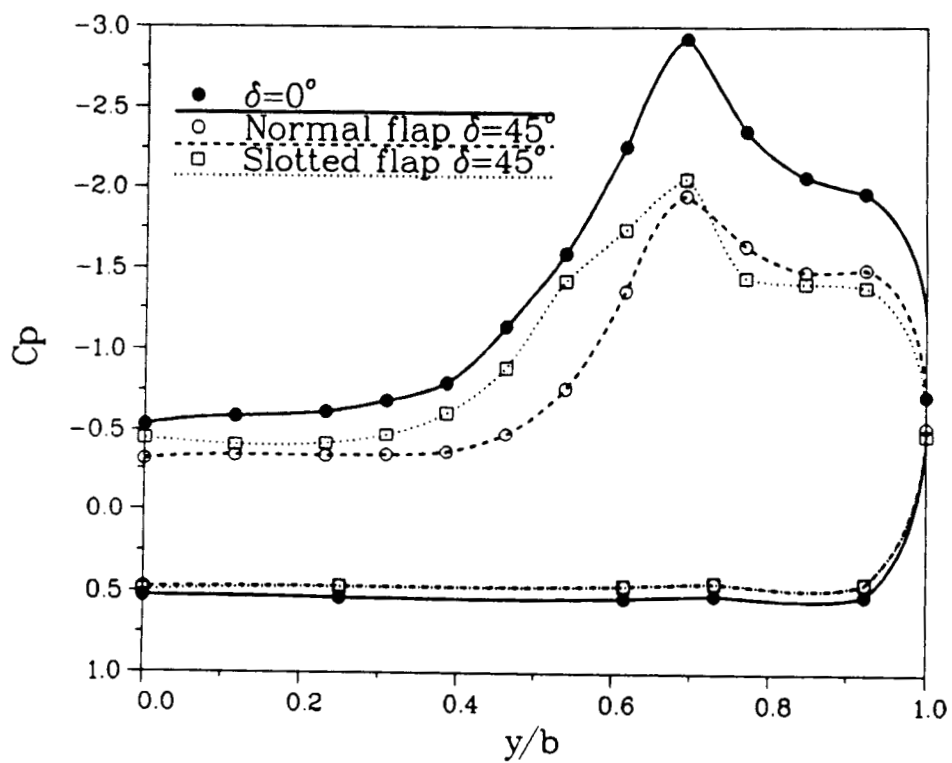


Fig. 14. Spanwise pressure distributions for the slotted flap.

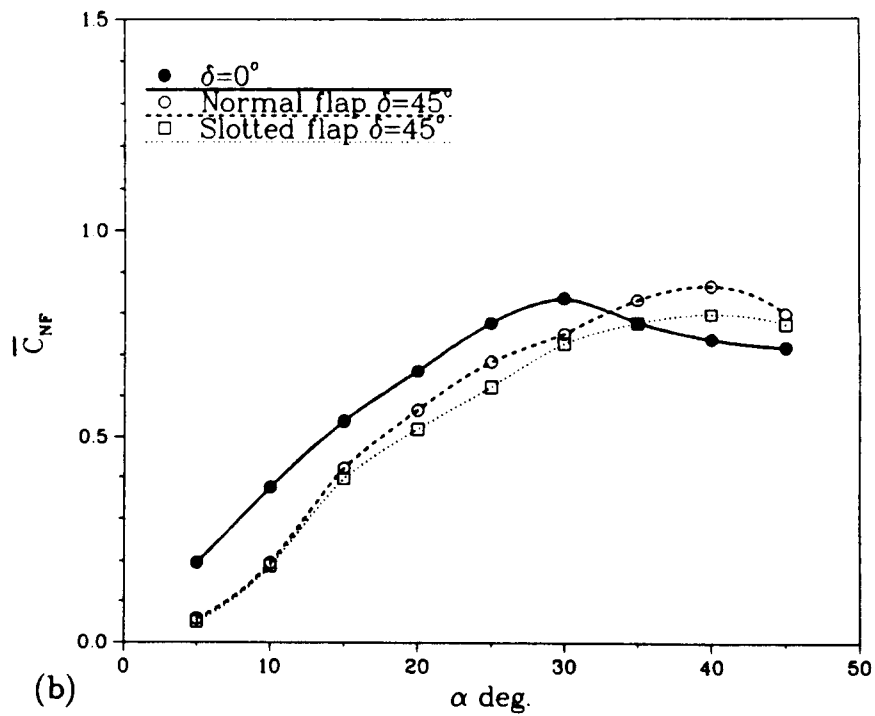
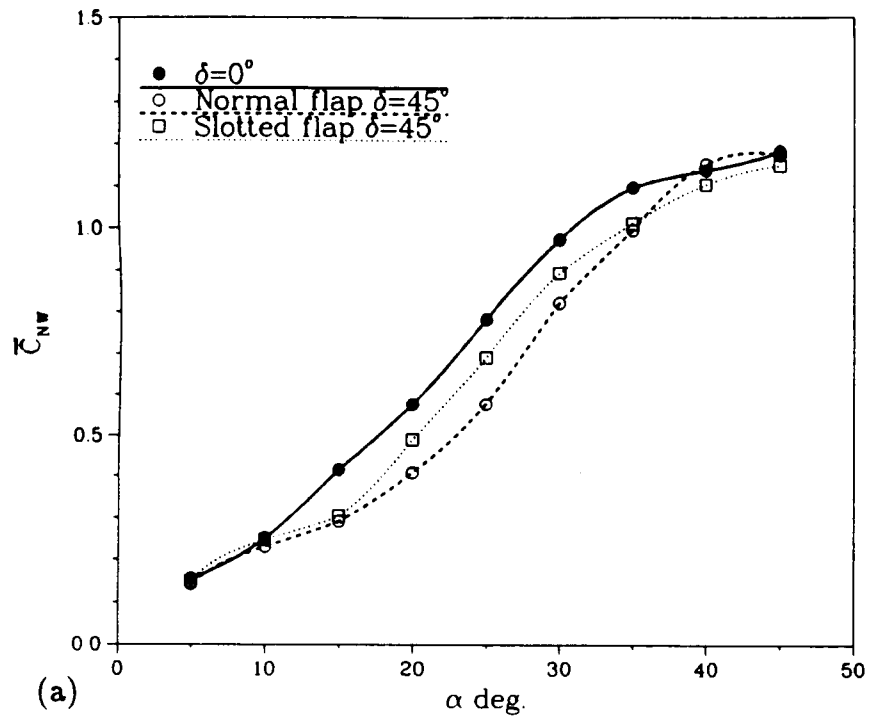


Fig. 15. Effect of the slotted flap on normal force coefficient.

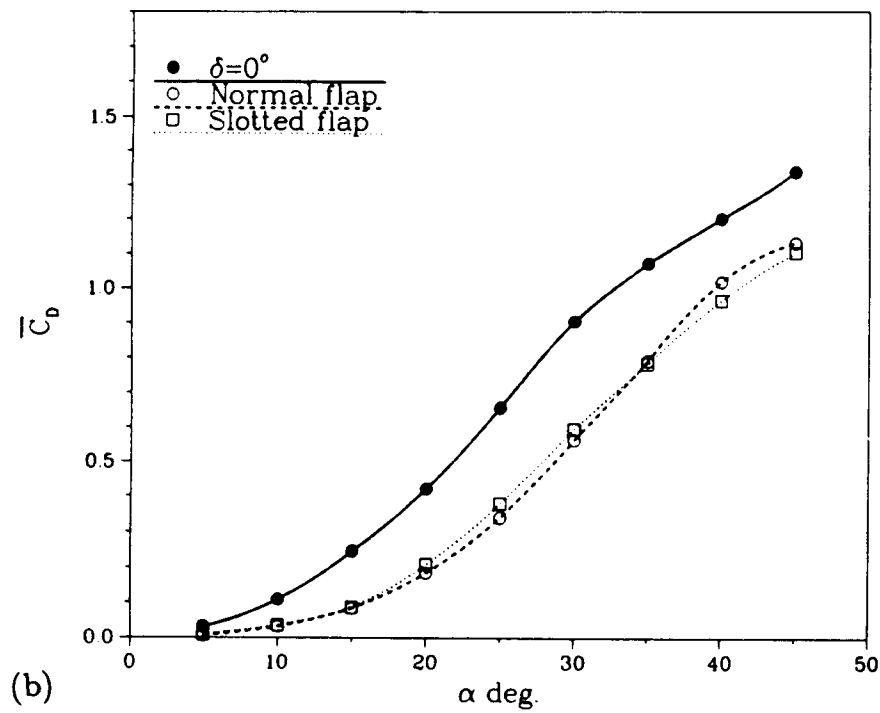
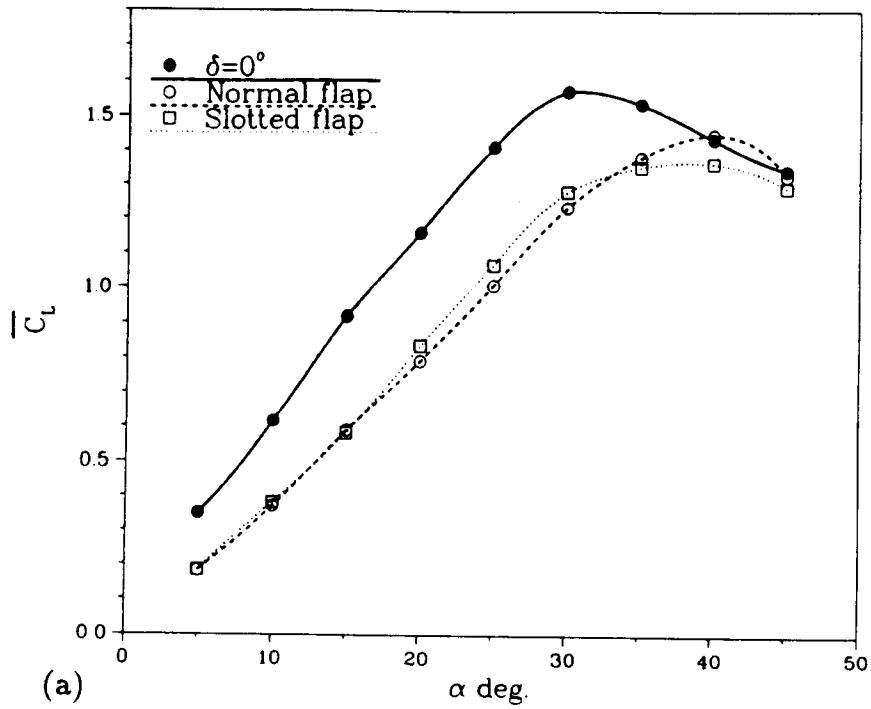


Fig. 16. Effect of the slotted flap on lift and drag coefficient.

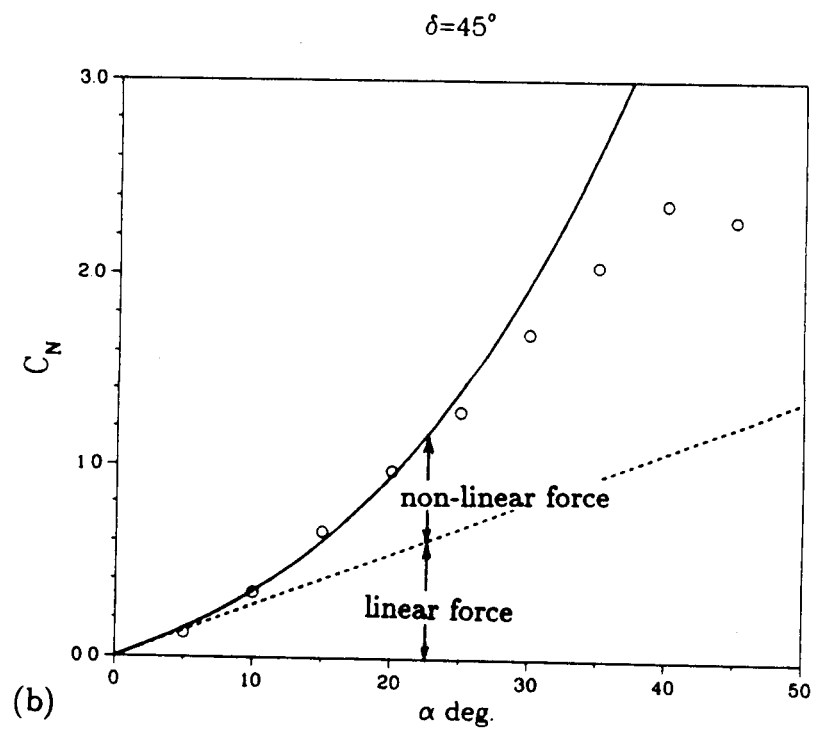
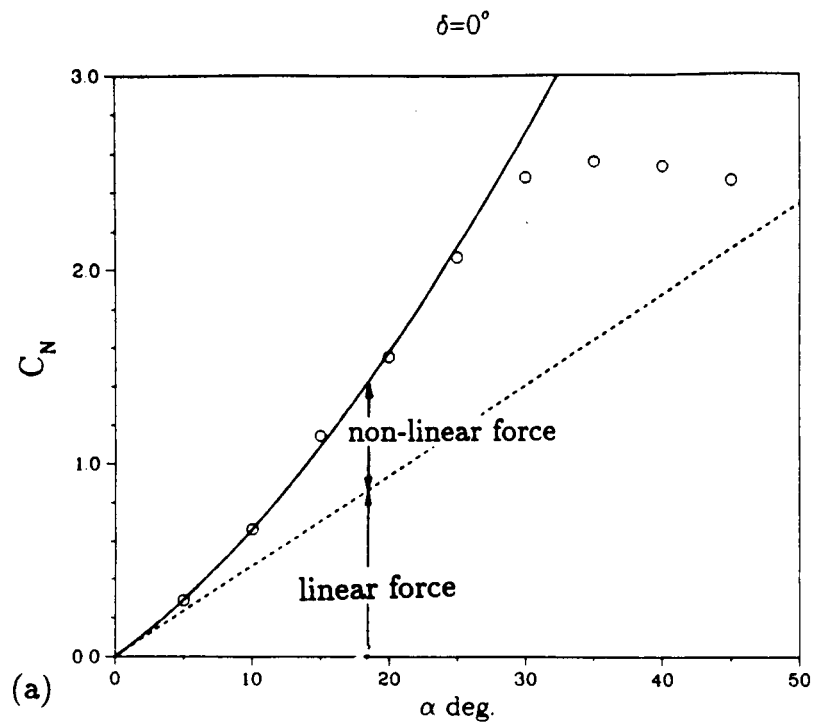


Fig. 17. Correlation of normal force coefficient

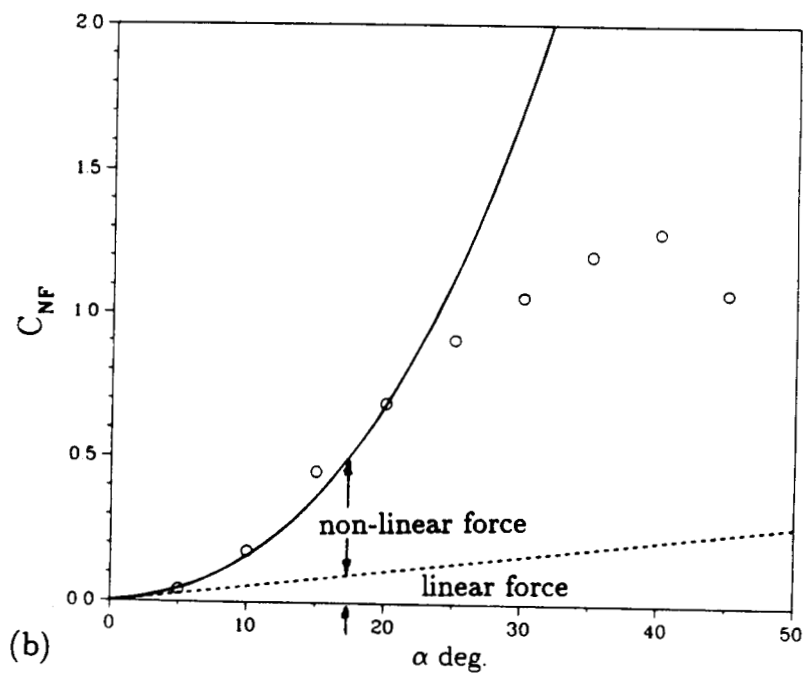
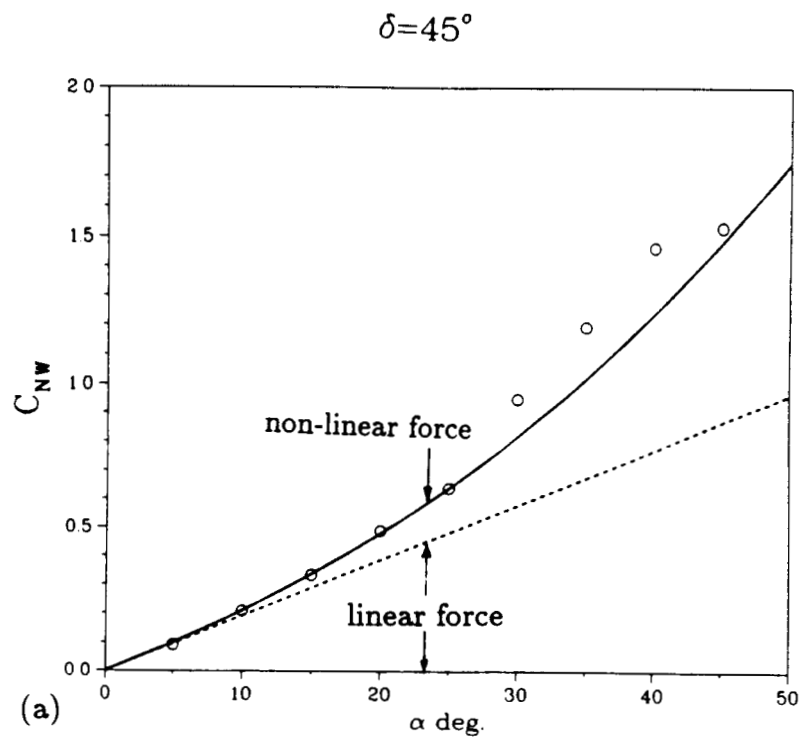


Fig. 18. Correlation of normal force coefficient for  $\delta = 45^\circ$ .

$\delta$	$k_1$	$k_2$	$p$
$C_N, \delta = 0^\circ$	1.05	5.06	1.74
$C_N, \delta = 45^\circ$	0.68	3.41	2.53
$C_{NF}, \delta = 45^\circ$	0.45	7.6	2.47
$C_{NW}, \delta = 45^\circ$	0.7	0.69	2.32

Table 1. Correltaion constants of the normal force in conical plane.